Functional analysis of single enzymes combining programmable molecular circuits with droplet-based microfluidics

Guillaume Gines, Rocıo Espada, Adèle Dramé-Maigné, Alexandre Baccouche, Nicolas Larrouy, Yannick Rondelez

Functional analysis of single enzymes combining programmable molecular circuits with droplet-based microfluidics

Guillaume Gines[1]*, Rocío Espada[1], Adèle Dramé-Maigné[1], Alexandre Baccouche[2], Nicolas Larrouy[1], Yannick Rondelez[1]

1. Laboratoire Gulliver, UMR7083 CNRS/ESPCI Paris-PSL Research University, 10 rue Vauquelin, 75005, Paris, France.
2. LIMMS, IRL 2820 CNRS-Institute of Industrial Science, The University of Tokyo; Meguroku, Tokyo, 153-8505, Japan

*corresponding author. Email: guillaume.gines@espci.fr

Abstract

The analysis of proteins at the single-molecule level uncovers heterogeneous behaviors that are masked in ensemble-averaged techniques. The digital quantification of enzymes traditionally involves the observation and counting of single molecules partitioned into microcompartments via the conversion of a pro-fluorescent substrate. This strategy based on linear signal amplification is limited to a few enzymes with sufficiently high turnover rate. Here we show that ~~by~~ combining the sensitivity of an exponential molecular amplifier with the modularity of DNA-enzyme circuits and droplet readout allows to specifically detect, at the single-molecule level, virtually any D(R)NA-related enzymatic activity. This strategy, denoted digital PUMA, is validated for more than a dozen different enzymes, including many with slow catalytic rate, and down to the extreme limit of apparent single turnover for *S. pyogenes* Cas9. Digital counting uniquely yields absolute molar quantification and reveals a large fraction of inactive catalysts in all tested commercial preparations. By monitoring the amplification reaction from single enzyme molecules in real-time, we also extract the distribution of activity among the catalyst population, revealing alternative inactivation pathways under various stresses. Our approach dramatically expands the number of enzymes that can benefit from quantification and functional analysis at single-molecule resolution. We anticipate digital PUMA to serve as a versatile framework for accurate enzyme quantification in diagnosis or biotechnological applications. These digital assays may also be utilized to study the origin of protein functional heterogeneity.

key words: single-molecule, digital detection, DNA circuits, molecular programming, enzyme stability

Enzymes are formidable catalysts that, besides their essential biological role, have profoundly transformed molecular sciences, biotechnologies and industrial processes. Nucleic acid-related enzymes, such as polymerases, nucleases, ligases and many more, have become essential components of the molecular biology toolbox. These are also important biomarkers of physio-pathological processes, playing an important role in DNA repair and metabolism or viral infections. Most enzymatic activities are measured via ensemble-averaged (bulk) biochemical assays to monitor the accumulation of the product of their catalytic activity. This is achieved using separative techniques such as electrophoresis or chromatography[1], or via spectroscopic[2] or electrochemical[3] methods. However, the enzymatic conversion of substrate to product is a linear process, making this approach insensitive, in comparison to nucleic acid quantification that benefits from nonlinear, e.g. exponential amplification strategies and routinely achieves sub-femtomolar LOD. In addition, the product accumulation rate is only a proxy for enzyme concentration, which is why many enzyme stocks are typically quantized only as arbitrary "units", representing observed bulk activity levels on a standardized assay. These "units" do not provide information on the actual molar concentration of catalysts nor their specific activity. Furthermore, bulk measurements hide precious information such as the catalytic diversity in the enzyme population, or the fraction of functional peptides, whereas it is known that these biopolymers exist in a variety of physical or chemical states, associated with various activities[4–6].

The possibility to detect the catalytic activity of individual enzymes was demonstrated 60 years ago for β-D-galactosidase confined in water-in-oil droplets.[7] Although widely polydisperse, these droplets were small enough for the conversion of a fluorogenic substrate by a unique enzyme to rapidly lead to fluorescent levels detectable by standard microscopy. This seminal work foreboded the emergence of digital bioassays, where single molecules are detected thanks to their isolation in microcompartments. One notable advantage of digital assay is calibration-free absolute quantification, contributing to its success in nucleic acid testing[8]. Since this initial demonstration, however, only a handful of additional enzymes have been detected using micro-compartmentalized digital approaches, including β-D-galactosidase[9–17], alkaline phosphatase[10,15,18–23], horseradish peroxidase[9,24–26], β-glucoronidase[27,28], scramblase[29], lactate dehydrogenase[30] and ATP synthase[31,32].

The restricted adaptability of digital readout for enzyme detection can be ascribed to several factors. Firstly, its dependence on the existence of a fluorogenic substrate that can be linked directly or indirectly[33] to the enzyme's activity. More crucially, digital readout is applicable only for enzymes with high turnover rates, allowing the linear accumulation of detectable product amounts by a single biocatalyst (Supplementary Note 1 and Figure S1).[34]

Here, we propose an alternative framework that combines molecular programming techniques and droplet microfluidics for the digital detection of a wide range of DNA and RNA processing enzymes, irrespective of their kinetic rates or the existence of a known fluorogenic substrate. Because it decouples the enzyme catalytic rate from the exponential signal generation, we demonstrate digital – single-molecule – counting even for "slow" enzymes, including nucleases, polymerase, ligase, kinase, N-glycosylases, down to the extreme case of an apparent single turnover enzyme such as Cas9 from *S. pyogenes*.[35,36] When compared to the total protein concentration, we evidenced that the fraction of active enzymes may vary over several orders of magnitude. Beyond the counting of functional biocatalysts, the real-time monitoring of the amplification reaction triggered from single molecules allows to access the catalytic diversity of an enzyme population. We show that the activity distribution of an isogenic enzyme pool responds differently to thermal or oxidative stresses, suggesting the coexistence of alternative aging pathway.

Results

Proof of principle with the nicking enzyme Nt.BstNBI. Our work leverages a generic molecular circuit, termed Programmable Ultrasensitive Molecular Amplifier (PUMA), that performs thresholded exponential amplification of a DNA signal[37], and which has been coupled to a variety of input activities[38–40]. It includes a conversion module, which connects the target (here an enzymatic activity), to the generation of a short DNA signal strand, and a DNA/enzyme amplification system, which ultimately yields a strong fluorescent readout. The latter is composed of three DNA templates: an autocatalytic template catalyzes the exponential replication of the signal strand using a DNA polymerase (Vent(exo-)) and a nicking enzyme (Nb.BsmI); a pseudotemplate deactivates a fraction of the signal strands and thus behaves as a catalytic drain to avoid nonspecific, target-independent amplification caused by leaky reactions[37]; a profluorescent reporter template hybridizes to the signal strands and, upon polymerization, generates a fluorescent signal.

We designed a conversion module to connect the amplification switch to the activity of a nicking enzyme, Nt.BstNBI (abbreviated NBI), used for diagnostics application (Figure 1A).[41] The stem-loop template catalyzes the linear production of the signal strand, which eventually triggers the exponential amplification. We monitored the reaction in real-time in presence of an increasing concentration of NBI (Figure 1B). As expected, the higher the target concentration, the faster the production of signal strands and consequently, the sooner the exponential amplification kicks in. The sensitivity of our approach in bulk is about 1 mu.mL^{-1} (milliunits per milliliter, that is about 400 fM of active enzyme, Table S4), i.e. four orders of magnitude lower than an assay based on the linear consumption of a profluorescent substrate (Figure 1C-D).

A versatile assay demonstrated over a dozen enzymes. By assembling a reaction cascade that links an enzymatic activity to the generation of the first signal strands, we validated a variety of sensing strategies for the detection of other nucleic acid-related enzymes (Figure 2A, see also Figure S6-S20). The detection of nucleases like RNASe (RNAseH2, Figure 2B) or AP-endonuclease (APE1, Figure 2C) is based on blocking the production of signal strand under the constitutive presence of NBI. The converter template includes the substrate of the enzyme (ribonucleotide or abasic site, respectively) that, upon endonucleolytic cleavage by the target enzyme, restores the linear production of signal strands by polymerization/nicking cycles. Adding one layer to the enzymatic cascade, we could detect uracil DNA glycosylase (UDG, Figure 2D) and the human Alkyl Adenine Glycosylase (AAG, Figure 2E), that excise uracil and hypoxanthine in DNA, respectively, leaving an AP-site for APE1 to incise. This enzymatic cascade strategy was adapted to restriction enzymes (BsmAI, Figure 2F), the poly(A) polymerase (PAP, Figure 2G), a DNA ligase and kinase (from T4 bacteriophage, Figure 2H-I) and to the RNA-guided endonuclease activity of Cas9 from *S. pyogenes* (SpyCas9, Figure 2J, Figure S22).

Certain enzymes present a catalytic activity that is incompatible with the PUMA conditions. This is the case for alkaline phosphatase (ALP) that hydrolyzes monoesters of phosphoric acid with a very broad substrate specificity, including deoxyribonucleotide triphosphate (dNTP). The dozens of micromolars of dNTP required for the PUMA reaction therefore prevents the direct sensitive detection of ALP. *Thermus thermophilus* argonaute (ttAgo) is a programmable DNA endonuclease that requires temperature above 65°C to be active, while the PUMA amplification reaction can be performed typically between 37 and 55°C. To circumvent this issue, we designed two-step assays (Figure 2K-L): the first step allows to accumulate the product of targeted enzymatic reaction while the second step complete the conversion of this product into the signal strands and their exponential amplification.

For these different bulk assays, the sensitivity is typically comprised between ~0.7 fM (5 $\mu u.mL^{-1}$) for PAP and a few dozens of picomolars for SpyCas9 (Table S4). This latter enzyme exhibits single turnover kinetic[42,43], which makes it particularly challenging to detect at subnanomolar level[35,44]. Noteworthily, we noted a qualitative correlation between the limit of detection of the assays and the turnover rate at steady state determined experimentally (Figure S2, Figure S3) or found in the literature (Figure S4). However, it should be noted that the PUMA assays are performed in non-saturating substrate concentration and with different experimental conditions. Although the assays work in a broad range of template concentrations, fine tuning of the experimental conditions is required to maximize the sensitivity while avoiding nonspecific amplification (summarized in the Supplementary note 2).

Assay specificity. We checked if the relatively long reaction cascades required for these ultrasensitive detections could still provide specific measurements of their target activity. 10 different PUMA assays targeting one of the enzymes listed above were spiked with 0.1 $u.mL^{-1}$ of each enzyme (except for Cas9 spiked at 5 nM) to generate the complete specificity matrix. The amplification reaction was then monitored in real-time (Figure 3 and Figure S23). We observed highly specific amplification reactions in all cases, where only the cognate activity is able to trigger the reaction. We noticed tenuous one-way crosstalk for the PNK enzyme, which tends to unspecifically initiate the amplification in non-cognate assays, though with a large delay compared to the target enzyme. This crosstalk corresponds to a concentration inferior to 1 $mu.mL^{-1}$ in the reference PNK assay (Figure 2I), i.e. a 100-fold specificity ratio. Moreover, the leakage in this case can be tracked down to the excision by PNK of the 3' blocking phosphate of the aT and prevented by substituting the phosphate group by an inverted deoxythymidine synthon (Figure S24).

Digital counting of single enzymes. Digital detection becomes feasible when the limit of detection in bulk assay falls below the concentration of a single enzyme within the microcompartment volume. Capitalizing on the enhanced sensitivity of PUMA-based assays (Table S4), we envisioned a general approach, referred as digital PUMA (dPUMA), for the counting of single enzymes (Figure 4A). To assess this, the NBI circuit was spiked with varying concentrations of the target enzyme, followed by partitioning into monodisperse microdroplets,

amplification and analysis of these droplets through end-point fluorescence microscopy (Figure 4B). By quantifying the fraction of positive droplets and assuming random, Poissonian partitioning (see Materials and Methods), we determined the concentration of active enzymes, which was found to be proportional to the initial input concentration across a broad dilution series, confirming the accurate digital detection of this enzyme (Figure 4C, Figure S25).

This dPUMA workflow is directly compatible with all one-pot assays, and was repeated for a variety of enzymes, showing absolute quantification of the active molecules in each case (Figure 4D). Strikingly, the digital readout revealed that the concentration of catalytically active enzyme was substantially lower than the total enzyme concentration (provided by the manufacturer), sometimes by several orders of magnitude (Figure 4E). After eliminating possible experimental artifacts – such as deactivation or loss of the enzymes during the emulsification process (Figure S26), or presence of large amount of contaminating proteins (Figure S27) – we concluded that the samples indeed comprised a large fraction of non-functional enzymes, which could originate from deactivation during protein production, purification and/or storage.

Characterizing the activity distribution. To further investigate the composition and evolution of an enzyme mixture, we evaluated the activity distribution of a pool of theoretically identical polypeptides (commercial NBI), using a real-time version of the dPUMA protocol (Figure 5). We emulsified samples of various enzyme concentration to measure the activity distribution at different Poisson parameters (λ). The amplification reaction was monitored in real-time (Figure 5A-D). The start time within each occupied droplet is used as a proxy of the enzymatic activity: the more active the enzyme, the sooner the amplification, an assumption that is legitimated by the monotonous relationship between At and enzyme activity in bulk measurements (Figures 1-2, see also Figure S28). From the Figure 5F, it appears that the amplification time at low λ (<2) is narrow, which allows to distinguish pikes of droplets of different occupancies (1, 2, 3 or 4 enzymes). We verified that the activity distributions were satisfyingly fitted by a sum of Gaussian functions with respective weights constrained by the Poisson frequencies expected from the measured value of λ in each sample. The agreement between droplet occupancy and the Poisson law proves that the low active fraction measured by the digital assay (Figure 4E) is not due to a non-Poissonian partitioning of the enzymes (which could happen for enzymes that aggregate or are bound to long stretches of genomic DNA[45]). Importantly, the start time distribution in droplets containing a single enzyme has a coefficient of variation of only 17 %, suggesting that the active enzyme pool has a rather uniform activity profile (Figure 5G). The mean start time as a function of droplet occupancy provides an internal calibration curve that allows to estimate the coefficient of variation on single enzyme activity measurements. We find it to be lower than 20 % in these conditions (Table S1).

Effect of physical versus chemical treatment of an enzyme population. To explore the origin of the inactive fraction, we assessed how the activity distribution is influenced under various stress conditions: either a physical stress, involving a heat-shock step; or chemical stress, using an oxidative treatment with hydrogen peroxide (cf. Material and Methods). For the first case, we observed an exponential decay of the active fraction of enzymes as the duration of the heat-shock is increased (Figure 6C). However, the activity distribution within the residual active fraction closely resembles that of the untreated sample (Figure 6D and Figure S29). This two-state behavior, where an enzyme is either fully active or entirely inactivated, is observed regardless of the heat shock temperature, as depicted in Figure S30. It aligns with the concept of catastrophic denaturation model, described in previous reports[7,22], where the heated enzyme experiences reversible conformational changes, until it reaches a tipping point and irreversibly unfolds[46].

In contrast, a distinct pattern emerged during the oxidative treatment: the fraction of active enzymes again decays as the concentration of H_2O_2 is increased, however, the start time distribution clearly deviates from that of the untreated sample: more single enzymes exhibit lower – yet measurable – activity when the oxidative stress is strengthened. A mild oxidative stress thus results in a fraction of inactive enzymes alongside a subpopulation of enzymes with intermediate activities, suggesting a mechanism where oxidized substates with diminished

activity are accessible before the full loss of activity. The oxidation of residue side chains outside of the active site may destabilize the catalytic pocket, affect substrate recognition, or reduce the stability of the scaffold[47]. Such broadened activity distribution was not observed in the untreated commercial samples (Figure 5F), suggesting that the inactive fraction of full-length polypeptide that they contain could be related to folding/aggregation issues rather than to chemical damages.

Conclusion

Capitalizing on nucleic acid amplification sensitivity, we propose a generic strategy for the detection of nucleic acid-related enzymes, pivotal in molecular biology, biotechnology and molecular medicine. One-pot assays are immediately transposable to a simple droplet readout, providing digital accuracy on the active enzyme count. Such digital format, relying on amplification from compartmentalized single-molecule triggering, decouples the assay time from the analyte concentration. With a single end-point readout after typically 1-2 hours of incubation, dPUMA offers comparatively fast and simple quantification, even for ultra-dilute samples. Reported enzymatic assays already more than double the number of enzymes that can benefit from single-molecule detection with simple tools (which was so far restricted to a handful of fast catalysts) and open the way to many more provided a tailored and specific conversion strategy. Of interest, CRISPR-Cas enzymes have gained attention owing to the breakthroughs they have triggered in gene editing[48] and diagnosis[49]. Cas nucleases such as Spy Cas9 are challenging to detect by standard methods because of the very slow release of the cleaved product, which makes the enzyme essentially single-turnover[42,43]. To the best of our knowledge, this is the first time that this enzyme, or any other single-turnover enzyme, is detected at the single-molecule level thanks to a digital readout. It promises a complementary method for probing Cas enzyme substrate specificity or the effect of mutations on the D(R)NA guide. In addition, enzyme not directly compatible with one-pot conditions (e.g. ALP or ttAgo) can still be specifically measured by separating the conversion step from the amplification step in a two-step assays. Their digital detection would require more complex microfluidics, including for example pico-injection[50] (e.g. for the addition of dNTPs, which act as competitive substrate and prevent ALP detection in a one-step assay) or droplet fusion[51] stages.

While PCR-based assay has brought nucleic acid testing to the front line of non-invasive disease monitoring from liquid biopsies[52,53], we can reasonably anticipate that the development of sensitive enzymatic testing could correspondingly enable the detection of traces of enzymatic activities. dPUMA was for example demonstrated for AP-endonucleases[54], DNA *N*-glycosylases[55] or alkaline phosphatases[56], all being important biomarkers in cancer monitoring and diagnosis of many other diseases such as liver dysfunction.

Intriguingly, our digital enzymatic assays unveiled a 10 to 100-fold difference between the total protein concentration and the active fraction for every tested enzymes. Such accurate quantification method can be deployed to guide the optimization of expression, purification and storage conditions for a broad range of DNA-modifying enzymes.[57]

Beyond the counting of enzymes, we demonstrated that the real-time monitoring of the amplification reaction from single enzyme isolated in microdroplets can be used to infer their relative activity, and extract activity distributions for large enzyme populations. In this approach, digital amplification is typically a consequence of multiple turnovers of a single enzyme, and may not reveal subtle single-turnover kinetic effects, for which complementary technique are needed[17,28]. We showed that heat-shocked enzymes exhibit a bimodal activity distribution indicative of a catastrophic denaturation mechanism. By contrast, oxidative decay reveals a distinctive, more spread activity pattern indicating the presence of oxidized intermediates with lower -but non-null- activity. In a broader context, the real-time dPUMA method allows the functional analysis of heterogenous enzyme samples, with significant implications in biotechnological or medical context. This utility is illustrated in the Supplementary Note 3, where we track the activity distribution of a genetically randomized pool of enzyme variants, submitted to a functional selection pressure via a directed evolution protocol[58]. This analysis

shows that the initial, randomly mutated pool of enzymes contains a substantial fraction of inactive and low-activity variants, which are efficiently removed by the *in vitro* selection process (Figure S31). Notably, the measurement of activity distributions was conducted directly from crude bacteria lysate, obviating the need for purification.

We therefore expect that dPUMA will become an essential tool to study the origin and impact of functional heterogeneity in enzyme populations[27,59,60]. The examination of expression noise (e.g. transcriptionally, translationally or post-translationally introduced diversity[61,62]) for enzymes produced from the same genetic carrier[21] or the fine tracking of activity distributions during a directed evolution campaign (i.e. for enzymes translated from genetic libraries), provide two fascinating prospects in this context.

Acknowledgements

We would like to thank the R&D department of New England Biolabs for providing us with the enzyme concentrations. We thank Nicolas Lobato-Dauzier, Anthony Genot and the platform FEMTO-ST (CNRS, Besançon) for providing the silicon-made incubation chambers. This work was supported by the European Research Council under the framework program H2020 for research and innovation (grant projects MoP-MiP, N°949493 and ProFF, N°647275) and the ANR Grant N°243063 MoBiDYC.

Author Contributions Statement

G.G. and Y.R. conceived the study and contributed to the design of experiments. G.G., R.E. A.D-M. and N.L. performed the experiments. A.B. designed the spy.Cas9 assay and produced the sgRNA. G.G., Y.R. and R.E. contributed to data analysis and interpretation. G.G. drafted the paper and all authors provided feedback.

Competing interests statement

G.G. and Y.R. are listed as inventor on a patent assigned to the CNRS, INSERM, ESPCI Paris, Université de recherche PSL and Université Paris Cité. All other authors declare no competing interest.

Figures

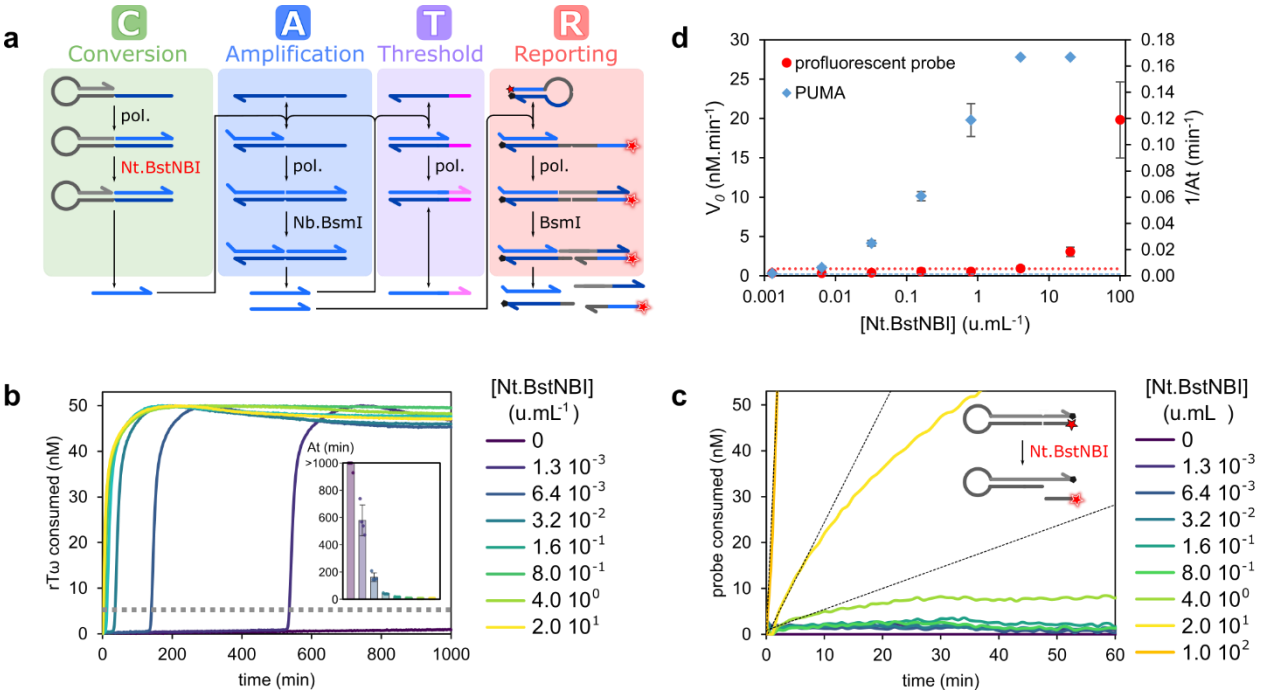

Figure 1. Proof of principle for the detection of Nt.BstNBI nickase activity. **a**, The isothermal amplification reaction leverages a 4-module DNA circuit. The conversion module is a self-priming template that includes a 5' output sequence complementary to the signal strand, just upstream to the target nicking enzyme recognition site, hence converting the enzymatic activity into the signal strand activator by polymerization/nicking cycles. The amplification module exponentially amplifies the signal strands. The threshold module dynamically drains out signal strands, setting an amplification threshold that prevents the system from self-igniting in absence of the target activity. The reporting module transduces the signal strands into a fluorescent readout. **b**, The amplification reaction is monitored in real-time for samples containing a varying concentration of NBI. The inset shows the amplification time (At, as mean value +/- SD (n = 3)), i.e. the time the fluorescence trace crosses a given threshold, corresponding to 10 % of the maximum fluorescence (dashed gray line). **c**, For comparison, we measured the enzymatic activity of NBI from the linear conversion of a profluorescent substrate (nbi-probe, Table S3) into a fluorescent product. The cleavage reaction at 55 °C of 500 nM of nbi-probe (~10 times higher concentration than K_m, Figure S2) is monitored in real-time for samples containing varying concentrations of NBI. The initial probe cleavage rates V_0 are extracted from the fit at t = 0 min (black lines). **d**, PUMA-aided assay (1/At) versus profluorescent probe (V_0). The data are plotted as the mean value +/- SD (n = 3). Dash lines represent the average negative control signal plus 3 times the standard deviation. For the PUMA assay, since nonspecific amplification is not observed for the negative control (the concentration of pT being set to absorb efficiently signal strands resulting from leaky reaction), the mean 1/At value is null.

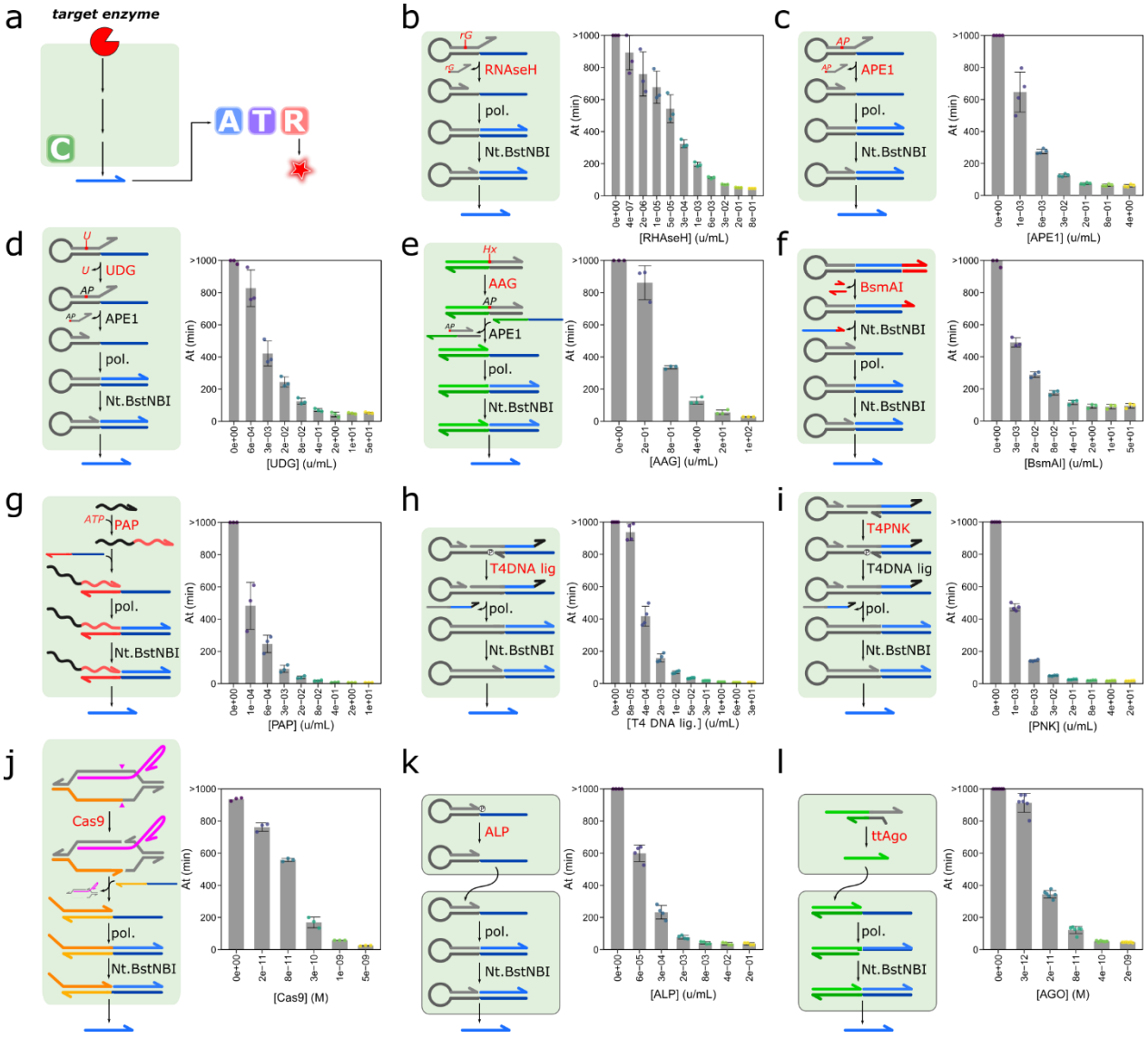

Figure 2. Generalization of the Programmable Ultrasensitive Molecular Amplifier (PUMA)-assisted detection assay over a dozen enzymes. **a**, All assays rely on the conversion of the targeted enzymatic activity into the signal strand that triggers the amplification reaction. **b**, For RNAse H detection, the stem of the self-priming conversion template is modified with a ribonucleotide (rG) and the polymerization is blocked with a protruding 3' polythimidylate extension, until hydrolysis of the enzyme substrate. **c**, A similar design is used for the detection of AP-endonuclease 1 (APE1), where the stem includes an abasic (AP) site that is cleaved by the target enzyme. **d**, Uracil DNA glycosylase (UDG) is detected by substituting the AP-site with a 2'-deoxyribouridine moiety, adding one more step to the enzymatic cascade: excision of the uracil base by the glycosylase introduces an abasic site that is further incised by APE1, eventually reactivating the production of signal strands. **e**, Alkyl adenine glycosylase (AAG) is revealed by inserting an inosine residue (hypoxanthine nucleobase, Hx) in a short double-stranded oligonucleotide. Upon excision by AAG and incision of the AP-site by APE1, the 5' part of the nicked strand dissociates spontaneously and is used as an input of a NBI-dependent template, which outputs the signal strand. **f**, For BsmAI restriction enzyme detection, its restriction site is appended to the 5' of the conversion template, which yields extended, non-amplifiable signal strand. The restriction of the extension of the converter template by BsmAI resumes the production of signal strands activators to be subsequently amplified. **g**, In Polyadenine polymerase (PAP) detection assay, the enzyme catalyzes the addition of a

polyadenine tail to the 3' extremity of a short RNA strand substrate, which therefore binds to the poly(T) input site of the conversion template, outputting the signal strand. **h**, T4 DNA ligase is detected using a split converter template substrate, whose signal strand production is restored upon templated ligation of the 5' phosphorylated and 3' hydroxyl extremities. **i**, T4 polynucleotide kinase (PNK) detection requires an unphosphorylated 5' end for PNK to add the missing phosphate, allowing the reaction cascade (ligation/polymerization/nicking) to proceed. By changing the substrate of this enzyme for a 3'-phosphated conversion template, its 3' exonuclease activity can be measured as well (Figure S21). **j**, Cas9 detection relies on the cleavage by this enzyme of its double-stranded DNA substrate in presence of the single guide RNA (sgRNA). The newly generated 3' end is used as an input of a converter template that linearly produces the signal strand by polymerization/nicking cycles. **k**, 2-step alkaline phosphatase (ALP) detection. In the first step, a self-primed conversion template, blocked for elongation by a 3' phosphate group, is dephosphorylated by ALP. Ten percent of this solution is then injected in the amplification mixture, where unphosphorylated conversion templates produce signal strands that trigger the amplification. **l**, 2-step tth Argonaute (ttAgo) detection. In the first step, ttAgo catalyzes the DNA-guided cleavage of a single-stranded DNA substrate. The product is converted into the signal strand in the second step amplification mixture. All data are plotted as the mean value of At +/- SD ($6 \geq n \geq 3$, cf. source data files). Error bars represent the standard deviation over three or more independent experiments.

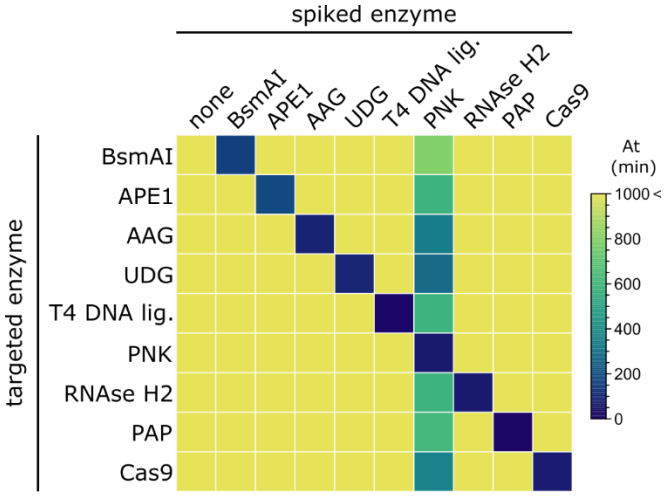

Figure 3. Specificity of the enzymatic assays. Heat map of the amplification time as a function of the conversion module and the spiked enzymes. The conditions of the assays are reported in Table S1.

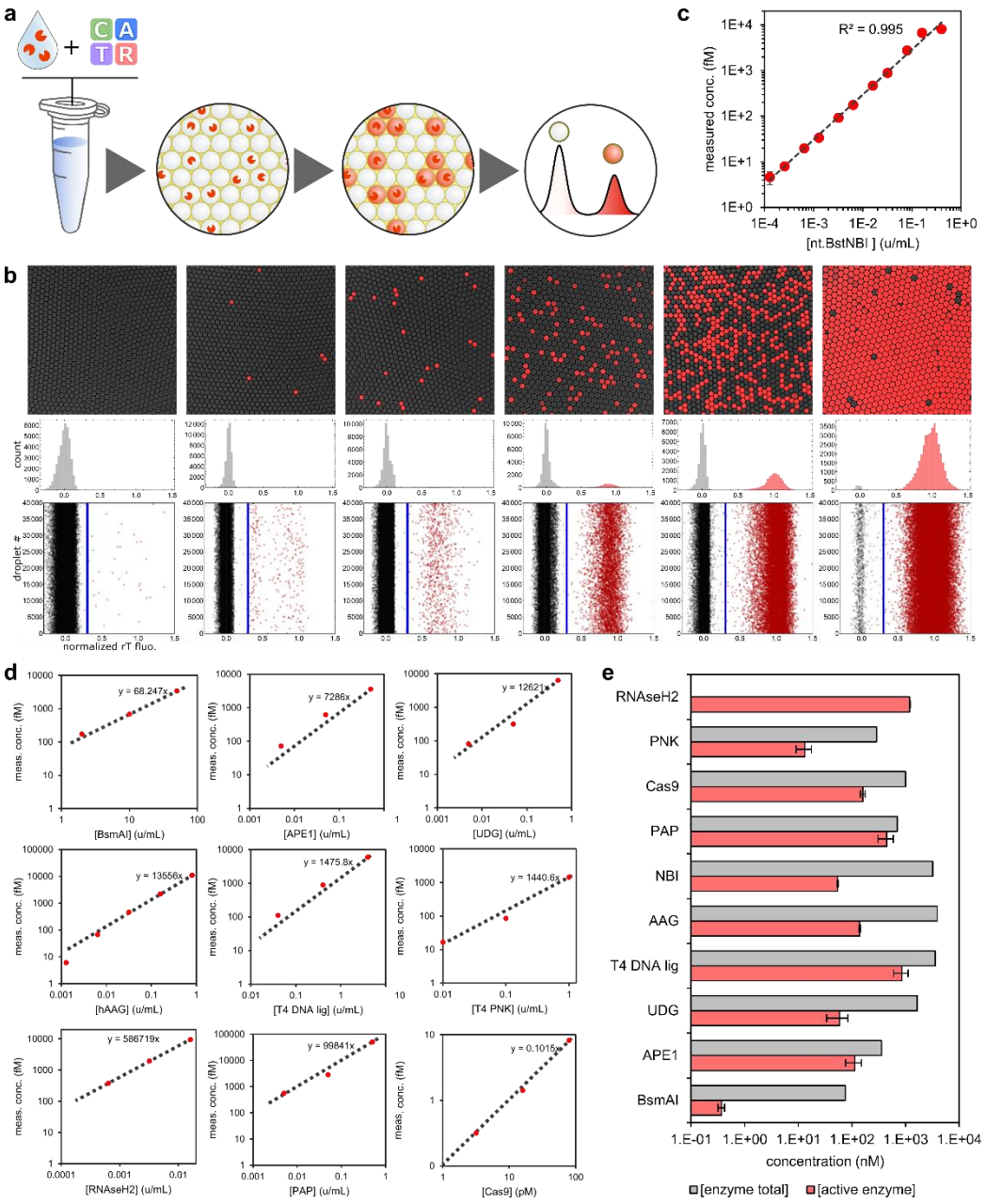

Figure 4. Digital detection of DNA-related enzymes. **a**, The workflow consists in distributing single enzyme molecules in water-in-oil microfluidic droplets, together with the cognate PUMA circuit. The emulsion is incubated to reveal the presence/absence of active enzyme by the amplification of a fluorescence signal. The active enzyme concentration is computed using the Poisson law from the fraction of positive compartments and droplet volume. **b**, Post-incubation microscopy snapshots and corresponding fluorescence distribution of the ~500 fL droplets generated from samples containing a varying concentration of the target enzyme NBI. Droplets above the dashed blue line (set to 30% of the normalized fluorescence intensity) are scored positive. **c**, Measured concentration of active NBI as a function of the spiked concentration in u.mL^{-1}. **d**, Concentration measured from the digital readout versus spiked concentration for various enzymes. **e**, Active (measured using digital PUMA assay) versus total (provided by the manufacturer) stock enzyme concentration (see Table S4 for the corresponding enzymatic activity). The active enzyme concentration and standard deviation were determined from independent digital measurements at three different enzyme dilutions.

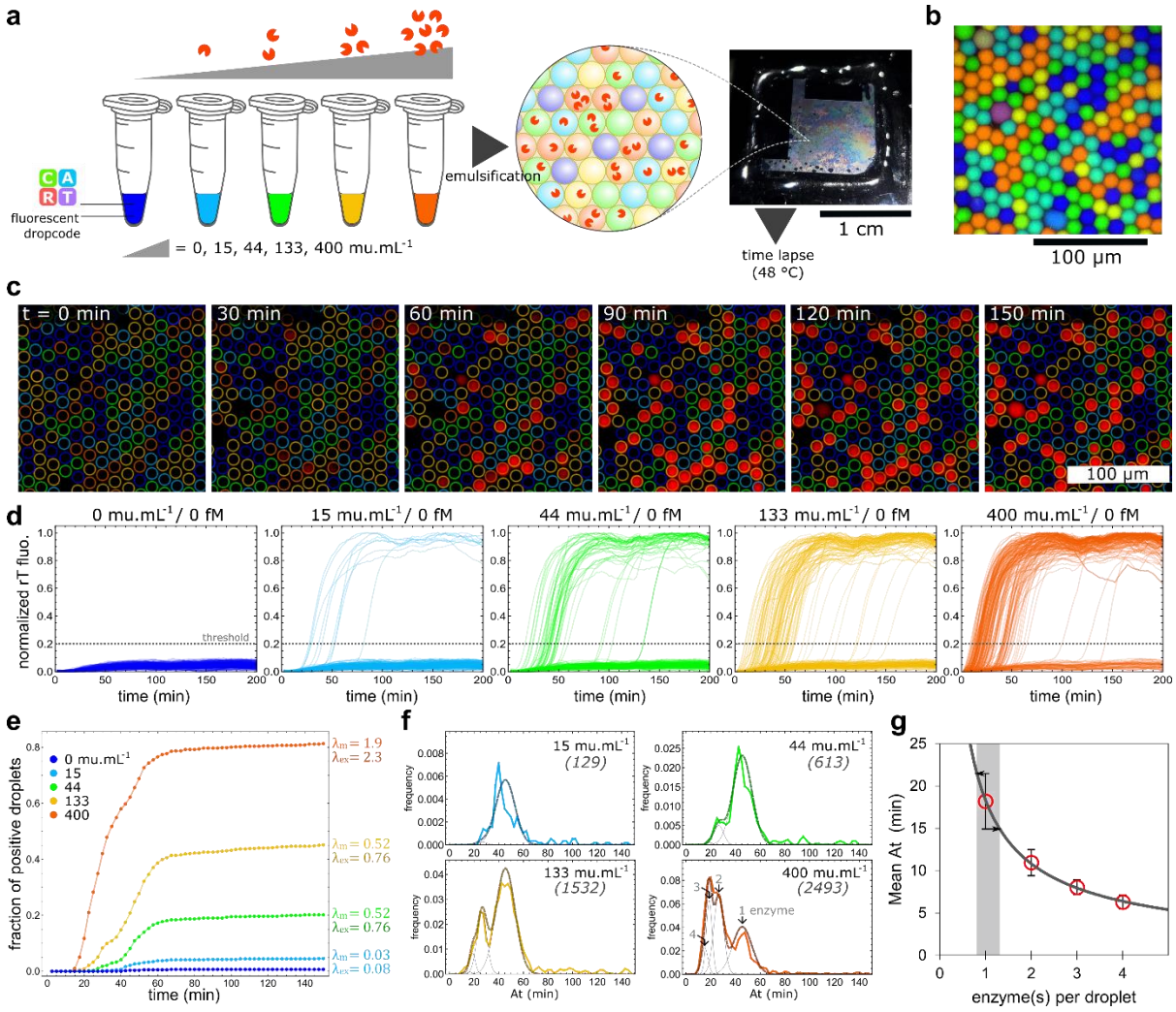

Figure 5. Activity distribution is assessed from time-lapse experiments. **a**, Samples containing various concentrations of untreated NBI were prepared each spiked with a combination of fluorescently-labeled dextrans that defines a dropcode. Following the serial emulsification of all samples in 1.8 pL droplets, the emulsions were mixed and injected in an imaging chamber carved in silicon and sealed with a glass cover slip. **b**, Composite microscopy snapshot of the barcoded droplets. **c**, Microscopy snapshots of the rT fluorescence. Droplets are circled with dropcode-specific colors. **d**, Time traces of the reporter template (rT) fluorescence for 200 droplets per sample. The fluorescence threshold for a droplet to be considered positive is indicated by the dash lines. The total enzyme activity (expressed as mu.mL^{-1}) and molar concentration of the active fraction are shown on the top. **e**, Fraction of positive droplets as a function of time. Poisson parameter (mean occupancy, λ) computed from the fraction of positive droplets at t = 150 minutes, λ_m, and expected from the spiked concentrations, λ_{ex}, are indicated on the right. **f**, Distribution of the start times. All data points were simultaneously fitted as a sum (dotted line) of four Gaussian functions (black thin lines, for 1, 2, 3 or 4 enzyme occupancy), assuming a Poisson distribution constrained by the computed lambda parameters. The number of starting droplets included in each distribution is indicated in parentheses **g**, Extracted fit parameter values (mean start time as dots and standard deviation as error bars, n = 4) as a function of the droplet occupancy. These data points can be fitted with a power function, used to estimate the standard deviation on the single enzyme activity (gray window).

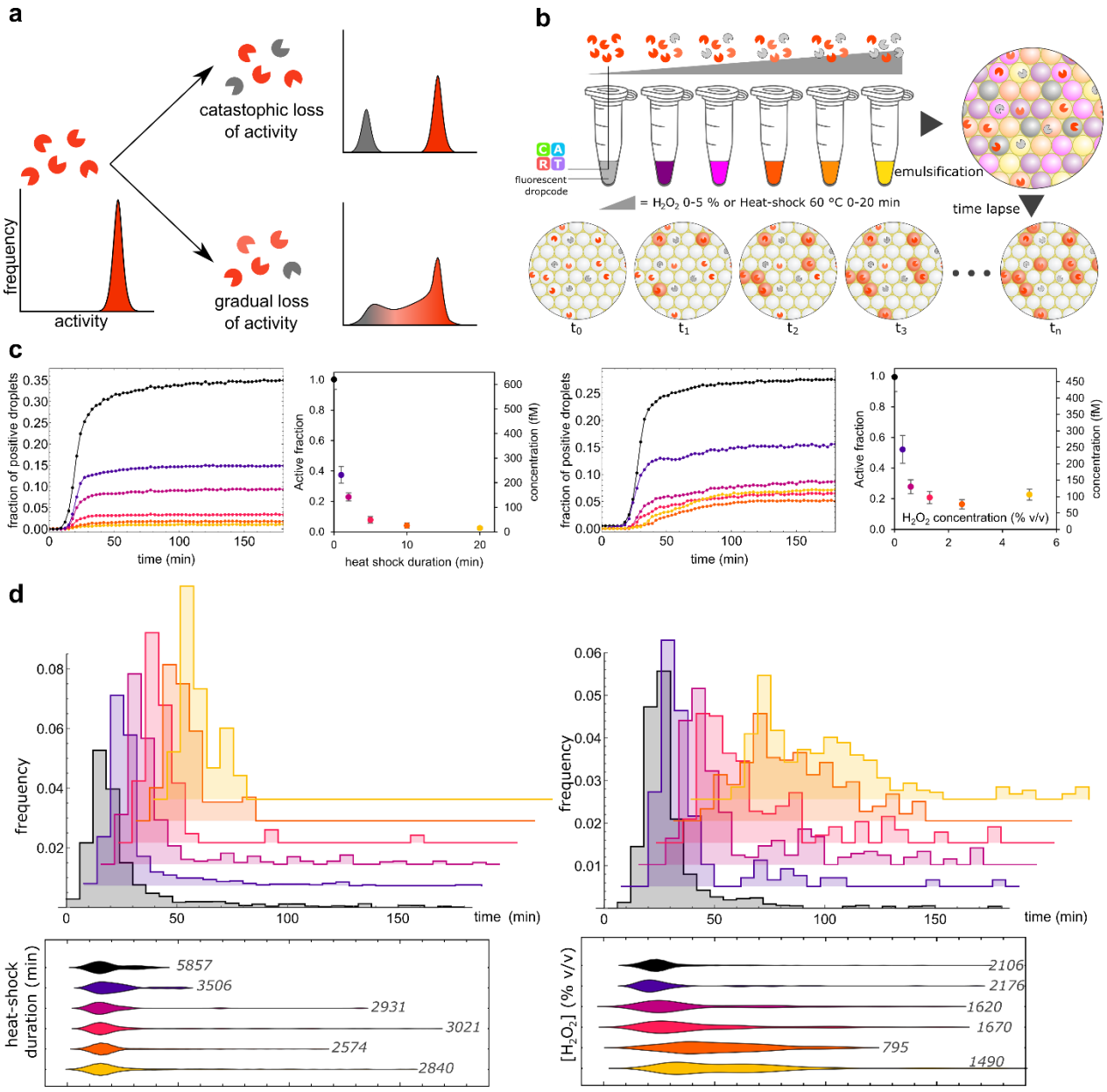

Figure 6. Study of functional heterogeneity of an enzyme population. **a**, The loss of activity of an enzyme may follow an all-to-none (catastrophic) path or a more gradual deactivation. **b**, The activity distribution of single NBI enzymes, subjected to an oxidative stress (various hydrogen peroxide concentrations for a 10-minute period) or heat shock (at 60 °C for various periods of time) is evaluated from the real-time analysis of the amplification reaction in droplets. **c**, Fraction of positive droplets as a function of time and end-point analysis (t = 180 min) for heat-shocked (left) and H_2O_2-treated (right) NBI (final concentration of ~400 fM, distributed in 900 fL droplets). Error bars on the active fraction/concentration correspond to the 95 % confidence interval. **d**, Probability distribution of the amplification start times (the sooner the amplification, the higher the activity). The lower droplet volume results in a higher concentration in loaded droplets, which explains the faster amplification times as compared to the Figure 5F. The number of droplets included in each distribution is indicated in italic.

References

1. Greenough, L. et al. Adapting capillary gel electrophoresis as a sensitive, high-throughput method to accelerate characterization of nucleic acid metabolic enzymes. Nucleic Acids Res 44, e15–e15 (2016).
2. Farag, N. et al. Folding-upon-Repair DNA Nanoswitches for Monitoring the Activity of DNA Repair Enzymes. Angewandte Chemie 133, 7359–7365 (2021).
3. Luo, X. & Hsing, I.-M. Immobilization-Free Electrochemical DNA Polymerase Assay. Electroanalysis 23, 923–926 (2011).
4. Boehr, D. D., Nussinov, R. & Wright, P. E. The role of dynamic conformational ensembles in biomolecular recognition. Nat Chem Biol 5, 789–796 (2009).
5. Henzler-Wildman, K. & Kern, D. Dynamic personalities of proteins. Nature 450, 964–972 (2007).
6. Leveson-Gower, R. B., Mayer, C. & Roelfes, G. The importance of catalytic promiscuity for enzyme design and evolution. Nat Rev Chem 3, 687–705 (2019).
7. Rotman, B. Measurement of activity of single molecules of beta-D-galactosidase. Proc. Natl. Acad. Sci. U.S.A. 47, 1981–1991 (1961).
8. Vogelstein, B. & Kinzler, K. W. Digital PCR. PNAS 96, 9236–9241 (1999).
9. Rondelez, Y. et al. Microfabricated arrays of femtoliter chambers allow single molecule enzymology. Nat Biotech 23, 361–365 (2005).
10. Ono, T., Ichiki, T. & Noji, H. Digital enzyme assay using attoliter droplet array. Analyst 143, 4923–4929 (2018).
11. Guan, Z. et al. A highly parallel microfluidic droplet method enabling single-molecule counting for digital enzyme detection. Biomicrofluidics 8, 014110 (2014).
12. Rojek, M. J. & Walt, D. R. Observing Single Enzyme Molecules Interconvert between Activity States upon Heating. PLOS ONE 9, e86224 (2014).
13. Rissin, D. M. & Walt, D. R. Digital Concentration Readout of Single Enzyme Molecules Using Femtoliter Arrays and Poisson Statistics. Nano Lett. 6, 520–523 (2006).
14. Liebherr, R. B. et al. Three-in-one enzyme assay based on single molecule detection in femtoliter arrays. Anal Bioanal Chem 407, 7443–7452 (2015).
15. Obayashi, Y., Iino, R. & Noji, H. A single-molecule digital enzyme assay using alkaline phosphatase with a cumarin-based fluorogenic substrate. Analyst 140, 5065–5073 (2015).
16. Gorris, H. H., Rissin, D. M. & Walt, D. R. Stochastic inhibitor release and binding from single-enzyme molecules. PNAS 104, 17680–17685 (2007).
17. English, B. P. et al. Ever-fluctuating single enzyme molecules: Michaelis-Menten equation revisited. Nat Chem Biol 2, 87–94 (2006).
18. Hsin, T.-M. & Yeung, E. S. Single-Molecule Reactions in Liposomes. Angewandte Chemie International Edition 46, 8032–8035 (2007).
19. Ueno, H., Kato, M., Minagawa, Y., Hirose, Y. & Noji, H. Elucidation and control of low and high active populations of alkaline phosphatase molecules for quantitative digital bioassay. Protein Science 30, 1628–1639 (2021).
20. Jiang, Y., Li, X. & Walt, D. R. Single-Molecule Analysis Determines Isozymes of Human Alkaline Phosphatase in Serum. Angewandte Chemie International Edition 59, 18010–18015 (2020).
21. Sakuma, M. et al. Genetic perturbation enhances functional heterogeneity in alkaline phosphatase. 2021.11.25.470051 Preprint at https://doi.org/10.1101/2021.11.25.470051 (2021).
22. Craig, D. B., Arriaga, E. A., Wong, J. C. Y., Lu, H. & Dovichi, N. J. Studies on Single Alkaline Phosphatase Molecules: Reaction Rate and Activation Energy of a Reaction Catalyzed by a Single Molecule and the Effect of Thermal DenaturationThe Death of an Enzyme. J. Am. Chem. Soc. 118, 5245–5253 (1996).
23. Sakuma, M. et al. Genetic Perturbation Alters Functional Substates in Alkaline Phosphatase. J. Am. Chem. Soc. (2023) doi:10.1021/jacs.2c06693.
24. Gorris, H. H. & Walt, D. R. Mechanistic Aspects of Horseradish Peroxidase Elucidated through Single-Molecule Studies. J. Am. Chem. Soc. 131, 6277–6282 (2009).
25. Ehrl, B. N., Liebherr, R. B. & Gorris, H. H. Single molecule kinetics of horseradish peroxidase exposed in large arrays of femtoliter-sized fused silica chambers. Analyst 138, 4260–4265 (2013).

26. Comellas-Aragonès, M. et al. A virus-based single-enzyme nanoreactor. Nature Nanotech 2, 635–639 (2007).
27. Liebherr, R. B., Renner, M. & Gorris, H. H. A Single Molecule Perspective on the Functional Diversity of in Vitro Evolved β-Glucuronidase. J. Am. Chem. Soc. 136, 5949–5955 (2014).
28. Jiang, Y. et al. Single-Molecule Mechanistic Study of Enzyme Hysteresis. ACS Cent. Sci. 5, 1691–1698 (2019).
29. Watanabe, R., Sakuragi, T., Noji, H. & Nagata, S. Single-molecule analysis of phospholipid scrambling by TMEM16F. PNAS (2018) doi:https://doi.org/10.1073/pnas.1717956115.
30. Tan, W. & Yeung, E. S. Monitoring the Reactions of Single Enzyme Molecules and Single Metal Ions. Anal. Chem. 69, 4242–4248 (1997).
31. Sakakihara, S., Araki, S., Iino, R. & Noji, H. A single-molecule enzymatic assay in a directly accessible femtoliter droplet array. Lab Chip 10, 3355–3362 (2010).
32. Watanabe, R. et al. Arrayed lipid bilayer chambers allow single-molecule analysis of membrane transporter activity. Nat Commun 5, 4519 (2014).
33. Ueno, H., Sano, M., Hara, M. & Noji, H. Digital Cascade Assays for ADP- or ATP-Producing Enzymes Using a Femtoliter Reactor Array Device. ACS Sens. (2023) doi:10.1021/acssensors.3c00587.
34. Noji, H., Minagawa, Y. & Ueno, H. Enzyme-based digital bioassay technology – key strategies and future perspectives. Lab on a Chip 22, 3092–3109 (2022).
35. Cox, K. J., Subramanian, H. K. K., Samaniego, C. C., Franco, E. & Choudhary, A. A universal method for sensitive and cell-free detection of CRISPR-associated nucleases. Chem. Sci. 10, 2653–2662 (2019).
36. Sternberg, S. H., Redding, S., Jinek, M., Greene, E. C. & Doudna, J. A. DNA interrogation by the CRISPR RNA-guided endonuclease Cas9. Nature 507, 62–67 (2014).
37. Montagne, K., Gines, G., Fujii, T. & Rondelez, Y. Boosting functionality of synthetic DNA circuits with tailored deactivation. Nature Communications 7, 13474 (2016).
38. Gines, G. et al. Isothermal digital detection of microRNA using background-free molecular circuit. Sci. Adv. (2020) doi:10.1126/sciadv.aay5952.
39. Shenshin, V. A., Lescanne, C., Gines, G. & Rondelez, Y. A small-molecule chemical interface for molecular programs. Nucleic Acids Research 49, 7765–7774 (2021).
40. Okumura, S. et al. Nonlinear decision-making with enzymatic neural networks. Nature 610, 496–501 (2022).
41. Li, Y. et al. Ultrasensitive Isothermal Detection of SARS-CoV-2 Based on Self-Priming Hairpin-Utilized Amplification of the G-Rich Sequence. Anal. Chem. 94, 17448–17455 (2022).
42. Richardson, C. D., Ray, G. J., DeWitt, M. A., Curie, G. L. & Corn, J. E. Enhancing homology-directed genome editing by catalytically active and inactive CRISPR-Cas9 using asymmetric donor DNA. Nat Biotechnol 34, 339–344 (2016).
43. Raper, A. T., Stephenson, A. A. & Suo, Z. Functional Insights Revealed by the Kinetic Mechanism of CRISPR/Cas9. J. Am. Chem. Soc. 140, 2971–2984 (2018).
44. Phaneuf, C. R. et al. Ultrasensitive multi-species detection of CRISPR-Cas9 by a portable centrifugal microfluidic platform. Anal. Methods 11, 559–565 (2019).
45. Zhang, X.-P. & Heyer, W.-D. Quality Control of Purified Proteins Involved in Homologous Recombination. in DNA Recombination: Methods and Protocols (ed. Tsubouchi, H.) 329–343 (Humana Press, 2011). doi:10.1007/978-1-61779-129-1_19.
46. Tanford, C. Protein Denaturation. in Advances in Protein Chemistry (eds. Anfinsen, C. B., Anson, M. L., Edsall, J. T. & Richards, F. M.) vol. 23 121–282 (Academic Press, 1968).
47. Berlett, B. S. & Stadtman, E. R. Protein Oxidation in Aging, Disease, and Oxidative Stress *. Journal of Biological Chemistry 272, 20313–20316 (1997).
48. Liu, G., Lin, Q., Jin, S. & Gao, C. The CRISPR-Cas toolbox and gene editing technologies. Molecular Cell 82, 333–347 (2022).
49. Phan, Q. A., Truong, L. B., Medina-Cruz, D., Dincer, C. & Mostafavi, E. CRISPR/Cas-powered nanobiosensors for diagnostics. Biosensors and Bioelectronics 197, 113732 (2022).
50. Abate, A. R., Hung, T., Mary, P., Agresti, J. J. & Weitz, D. A. High-throughput injection with microfluidics using picoinjectors. Proceedings of the National Academy of Sciences 107, 19163–19166 (2010).

51. Mazutis, L. & Griffiths, A. D. Selective droplet coalescence using microfluidic systems. Lab Chip 12, 1800–1806 (2012).
52. Mattox, A. K. et al. Applications of liquid biopsies for cancer. Science Translational Medicine 11, eaay1984 (2019).
53. Heitzer, E., Haque, I. S., Roberts, C. E. S. & Speicher, M. R. Current and future perspectives of liquid biopsies in genomics-driven oncology. Nat Rev Genet 20, 71–88 (2019).
54. Abbotts, R. & Madhusudan, S. Human AP endonuclease 1 (APE1): From mechanistic insights to druggable target in cancer. Cancer Treatment Reviews 36, 425–435 (2010).
55. Collins, A. R. & Gaivão, I. DNA base excision repair as a biomarker in molecular epidemiology studies. Molecular Aspects of Medicine 28, 307–322 (2007).
56. Zaher, D. M. et al. Recent advances with alkaline phosphatase isoenzymes and their inhibitors. Archiv der Pharmazie 353, e2000011 (2020).
57. Sachsenhauser, V. & Bardwell, J. C. Directed evolution to improve protein folding in vivo. Current Opinion in Structural Biology 48, 117–123 (2018).
58. Dramé-Maigné, A. et al. In Vitro Enzyme Self-Selection Using Molecular Programs. ACS Synth. Biol. (2024) doi:10.1021/acssynbio.3c00385.
59. Xue, Q. & Yeung, E. S. Differences in the chemical reactivity of individual molecules of an enzyme. Nature 373, 681–683 (1995).
60. Craig, D. B. et al. Differences in the Average Single Molecule Activities of E. coli β-Galactosidase: Effect of Source, Enzyme Molecule Age and Temperature of Induction. J Protein Chem 22, 555–561 (2003).
61. Tawfik, D. S. Messy biology and the origins of evolutionary innovations. Nat Chem Biol 6, 692–696 (2010).
62. Willensdorfer, M., Bürger, R. & Nowak, M. A. Phenotypic Mutation Rates and the Abundance of Abnormal Proteins in Yeast. PLOS Computational Biology 3, e203 (2007).

Materials and Methods

Materials

All oligonucleotides were ordered from Biomers, Eurofins Genomics or Integrated DNA Technologies (IDT). gBlock for single guide RNA synthesis (Spy Cas9 detection) was obtained from IDT. Sequences are summarized in Table S3. Molecular program enzymes Nt.BstNBI, Ven(exo-), Nb.BsmI, BsmI were purchased from New England Biolabs (NEB). TtRecJ 5'-3' exonuclease was expressed and purified in house according to a previously described protocol[63]. A dilution at 860 nM from the stock in Diluent A (NEB) supplemented with 0.1% TritonX-100 (Sigma-Aldrich) was prepared and stored at -20°C. For the target enzymes, Nt.BstNBI (catalog number R0607L, batch number 0401804), APE1 (M0282S, 0041610), hAAG (M0313S, 0021010), UDG (M0280S, 0121704), BsmAI (R0529S, 10025061), E.Coli PAP (M0276S, 10041074), T4 DNA ligase (M0202M, 1221707), T4 PNK (M0201S, 0921505), Spy Cas9 (M0386S, 10084278) and ttAgo (M0665S, 10092699) were purchased from NEB. RNAse H2 (11-03-02-02, 233682) and Alkaline Phosphatase (*E.Coli* C75, 2120A, AJE1047A) were obtained from IDT and Takara Bio., respectively. For parallelized droplet generation and analysis, fluorescently-labelled dextrans (ThermoFisher Scientific) were chosen from dextran CascadeBlue 10000 anionic fixable (cat. #D1976), dextran fluorescein 500000 anionic fixable (cat. #D7136), dextran AlexaFluor 488 (cat# D34682), dextran AlexaFluor 555 (cat# D34679) and dextran TexasRed 70000 neutral (cat. #D1830).

Single guide RNA transcription

sgRNA was encoded in a gBlock containing a T7 promoter. The transcription mixture contained 1X RNAPol reaction buffer (40 mM Tris-HCl pH 7.9 at 25°C, 6 mM $MgCl_2$, 1 mM DTT, 2 mM spermidine), 5 nM gBlock, 500 µM of each rNTPs (ThermoFisher Scientific), 1 $u.\mu L^{-1}$ of RNAse inhibitor murine (NEB cat. #M0314), 1X SyBr Green II (ThermoFisher Scientific) and 5 u.µL-1 of T7 RNA polymerase (NEB cat. #M0251). The reaction

was incubated at 34 °C for 8 hours. The sgRNA was aliquoted and stored without any further purification at -20°C. A 1000-fold dilution of the sgRNA is used in the Cas9 detection assay (Figure S20).

PUMA reaction mixture preparation

All reaction mixtures were assembled at 4°C. The 1X amplification buffer common to all assays contains 20 mM Tris-HCl pH 8.9, 10 mM $(NH_4)_2SO_4$, 40 mM KCl, 10 mM NaCl, 10 mM $MgSO_4$, 25 µM each dNTP, 0.1 % (w/v) synperonic F104, 2 µM netropsin. For one-pot assays, a master mix was prepared comprising the 1X reaction buffer, the nucleic templates (the target-specific conversion module, the autocatalytic template, pseudotemplate and reporter template), 200 µg.mL^{-1} BSA (NEB, cat. #B9000S) 300 u.mL^{-1} Nb.BsmI, 70 u.mL^{-1} Vent(exo-), 13 nM ttRecJ, 7 u.mL^{-1} BsmI and 10 u.mL^{-1} Nt.BstNBI (except for the detection of this enzyme). Conditions specific to each assay are reported in Table S1. The master mix is distributed, and the target enzyme spiked. The target enzyme is diluted in 200 µL tubes (VWR cat. #20170-012) in the 1X amplification buffer supplemented with 200 µg.mL^{-1} BSA, as followed. 1 µL of enzyme is transferred in 19 µL of buffer using a 0.1-10 µL low retention filter tip (Eppendorf cat. #0030078632 or Corning cat. #4135). With a second new tip, a serial dilution is realized by transferring 2 µL to 8 µL of buffer (cf. Figure S32 for the carry over effect related to using the same tip to perform the whole dilution). Using a third tip, the enzyme is spiked in the master mix from the lowest to the highest concentration. Following an optional preincubation step (Table S1), samples are incubated at 48 °C (or 50 °C for Cas9 detection assay) in a CFX96 touch instrument (Bio-Rad) and the fluorescence monitored in real-time. For digital assays, samples are emulsified prior to the (pre)incubation step (cf. below).

Two-step assays from this work include the detection of ALP and ttAgo. For ALP, the first step consisted in assembling 5 µL samples containing the target enzyme, 1X of ALP reaction buffer (50 mM Tris-HCl pH 9.0, 1 mM $MgCl_2$), 200 µg.mL^{-1} BSA and 4 nM of the substrate ALPtoω. The dephosphorylation proceeded for 1 h at 30 °C. In the second step, 5 µL of master mix was added with final concentrations identical to the one-step assays and the amplification reaction is monitored in real-time at 48 °C. The first step in ttAgo involved DNA-guided cleavage of a single-stranded DNA substrate (Agotoα). This step was performed in 10 µL samples containing 1 X ThermoPol reaction buffer (NEB, 20 mM Tris-HCl pH 8.8 at 25°C, 10 mM $(NH_4)_2SO_4$, 10 mM KCl, 2 mM $MgSO_4$, 0.1% Triton X-100), 200 µg.mL^{-1} BSA, 0.6 nM Agotoα and 10 nM gDNA (DNA guide). Sample were incubated for 5 hours at 70 °C and 3 µL was transferred to a tube containing 7 µL of mastermix. Templates, enzymes and buffer final concentrations were identical to the one-step assays, with the addition of 0.5 nM of αtoω that converts the output product of the cleavage reaction into the amplified ω sequence.

Linear signal amplification for the detection of NBI

A hairpin-shaped profluorescent probe (nbi-probe-Cy5, cf. Table S3) containing the nicking recognition site was designed so that the quencher moiety spontaneously dehybridizes after cleavage. The assay was conducted in 1X commercial buffer (50 mM Tris-HCl, pH 7.9, 10 mM $MgCl_2$, 100 mM NaCl, 100 µg.mL^{-1} BSA) with 500 nM of the probe. Samples were spiked with a varying concentration of the target enzyme and the product formation at 55 °C was monitored in real-time in a CFXtouch 96 (Bio-Rad). Initial velocities were extracted by fitting the first five minutes of the reaction with a linear regression.

Polyacrylamide gel electrophoresis

Denaturing PAGE analysis was performed using 15 % TBE-urea gel (Invitrogen). About 5 µL of the enzyme stock (0.4 µL for T4 DNA ligase, cf. Table S4) was mixed with 2.5 µL of NuPAGE loading buffer, completed to 10 µL with deionized water and heated for 5 minutes at 95 °C prior to gel loading. The gel was run at 120 V for 1 hour in an XCell SureLock Mini-Cell (ThermoFisher) with 1X TBE running buffer. The gel was subsequently stained with Instant Blue Coomassie protein stain (abcam) and imaged on a scanner HP LaserJet Pro MFP.

Microfluidic droplet generation

Sample partitioning was performed by a step-emulsification process using either a one-inlet or 2-inlet disperse phase devices. The continuous phase consisted in a fluorinated oil (HFE Novec 7500, 3M) supplemented with 1 % w/w fluorosurfactant (Emulseo). Device master molds were prepared using standard soft-lithography techniques. Briefly, a photoresist (SU-8, MicroChem Corp.) was spin-coated to the desired height on a 4-inch dehydrated silicon wafer, followed by UV exposure through the nozzle and filter mask phototraced on a transparent film (Selba S.A., Switzerland). Following development in propylene glycol methyl ether acetate, the operation (spin-coating, exposure, development) was repeated to include the rest of the channels. The mold was aligned with the mask using a MJB4 instrument (SUSS MicroTec, Germany). Devices were replicated from the master mold using PDMS 10:1 base/curing agent (Sylgard 184, Dow Corning). After baking 1 h at 70°C, the PDMS slab was peeled off, inlet and outlet drilled using 1.5 mm biopsy puncher (Integra Miltex), the replica was bound to a 1 mm thick glass slide (Paul Marienfeld GmbH & Co) using oxygen plasma surface activation and the chip was baked for 5 hours at 200 °C. Samples and oil were connected to the chip using PTFE tubing 200 µm ID (Cluzeau Info Labo, France) and injected using a pressure-based flow controller (MFCS EZ pump, Fluigent, France). Droplets are collected in a pipet tip plugged to the outlet.

Digital assays

One-inlet devices were used for the digital detection of NBI, APE1, RNAse H2, BsmAI and Spy Cas9 with no change in the sample preparation. Two-inlet devices were used for the digital detection of AAG, UDG, PAP, T4 DNA ligase and T4 PNK, because they are expected to activate a certain amount of conversion templates at room temperature, prior to the encapsulation, which would eventually trigger the amplification reaction even in droplets that do not contain active enzyme. To avoid early activation, we separated the enzymes and the oligonucleotides in 2 mixtures: the first mixture contained 1X amplification buffer the templates (sT, aT, pT, rT) and 200 µg.mL^{-1} BSA; the second mixture contained 1X amplification buffer, the molecular program enzymes, the target enzyme, 200 µg.mL^{-1} BSA and optionally the *dropcode* (cf. below).

To speed-up the emulsification and analysis process we optionally resorted to an off-chip sample changer device, previously reported[64]. In that case, distinct *dropcodes* — combinations of fluorescently-labelled dextran molecules each at a final concentration of 0-400 nM — were spiked in each sample prior to emulsification. All samples were emulsified for 3 minutes each and collected in a single tube. Emulsions were incubated in a CFXtouch 96 followed by microscopy imaging.

H_2O_2-treated and heat-shocked NBI

Oxidative treatment was performed on a 50-fold dilution of NBI in ultrapure water (stock concentration of active enzyme estimated at 100 nM), supplemented with a varying concentration of hydrogen peroxide (30 % solution, Sigma Aldrich) and incubated at 4 °C for 20 minutes. Heat shock treatment was performed on a on a 50-fold dilution of NBI in ultrapure water supplemented with 10 nM of nbitoω for different periods of time at 60 °C.

H_2O_2-treated or heat-shocked enzymes were subsequently diluted 500 times in the amplification buffer with 200 µg.mL^{-1} BSA and spiked at 10 % in the amplification mixture (final concentration ~400 fM). H2O2 has been shown to have little effect on the molecular program at such dilution (Figure S33). Dropcoded samples were partitioned in water-in-oil droplets as described above. To evaluate the activity distribution, the amplification reaction in droplets was monitored in real-time using time lapse imaging (cf. below).

End-point imaging

Following incubation, emulsions were imaged in end-point by microscopy as previously described[38,64]. In brief, a glass slide and coverslip were hydrophobized with Novec 1720 (3M). Polystyrene beads of a diameter close to the droplet size were placed in the four corner of the coverslip and used as spacer to control the thickness of the droplet monolayer. The chamber was sealed using an epoxy glue (Sader) and imaged thanks to an

epifluorescence microscope (Nikon Eclipse Ti) equipped with a motorized stage, a camera Nikon DS-Qi2, a CoolLed pE-4000 illumination source, a filter set (Semrock, DyLight405-C, FITC-3540C, Cy3-4040C, mCherry-C and LF635/LP-B) and a 20 x apochromatic objective (N.A. 0.75, WD 1.0). False color images were generated using the open-source ImageJ software.

Time lapse imaging

For time lapse analysis, microfabricated silicon chambers (1 square centimeter with a depth of 10 μm) were used according to a previously reported protocol[65]. Alternatively, the silicon chamber can be replaced by a thin bottom glass slide (44 x 70 mm, Menzel-Gläser), The silicon chamber or bottom glass slide and a 15x15 mm coverslip were treated with Aquapel or Fluo-ST1 (Emulseo) and thoroughly rinsed with deionized water. When using bottom glass slide, a few drops of 10 μm polystyrene particles (Polysciences, cat# 17136) were let to dry and serve as spacers between the bottom slide and the coverslip. Once filled with the emulsion (which takes 1-2 minutes), the chamber was sealed with an epoxy glue (Sader) and mounted on a heating plate (Tokai Hit). A 10 μL drop of mineral oil (Sigma-Merk) was added between the heating plate and the silicon chamber to maximize thermal contact. These operations were performed at room temperature. After setting the heating plate to 48 °C, it took about 10 minutes for the focus to be stable, after what the image acquisition was started through the ND acquisition interface of the microscope software (NIS).

Droplet analysis

Droplet images were analyzed with a custom-made Mathematica script (Wolfram) as previously described[64]. Briefly, droplets were segmented either using the brightfield image (end-point imaging in glass-made chambers) or dropcode images (time lapse imaging in silicon-made chambers, incompatible with transmission microscopy). For each droplet, the fluorescent of the dropcode channels and the reporter template channel was extracted. The different droplet populations were sorted according to their dropcode where necessary, and positive/negative droplets counted according to a fluorescence threshold set on the normalized reporter template fluorescence. Active enzyme concentration ($[ez]_A$) was computed assuming an initial Poisson distribution using the formula:

$$[ez]_A = \frac{-\ln(1 - F_{pos})}{N_A . V} \quad (1)$$

, where F_{pos} is the fraction positive droplet and $-\ln(1 - F_{pos})$ is the Poisson parameter, and N_A is the Avogadro number and V is the droplet volume.

For time lapse analysis, droplets were tracked using a nearest neighbor search algorithm (from the frame n to n+1), based on the XY coordinate and the three dropcode fluorescence values. This allowed to reconstruct the time traces of the rT fluorescence. Amplification times correspond to the time it takes for the time trace to reach 20 % of its maximum fluorescence. Activity distributions (Figure 5F) were fitted with a sum of four Gaussian functions:

$$\sum_{k=1}^{4} \frac{1}{a_{t_k} . CV_k . \sqrt{2\pi}} * \frac{\lambda^k}{k!} e^{-\lambda} * e^{-\frac{1}{2}\frac{(a_{t_k} - t)^2}{(a_{t_k} . CV_k)^2}} \quad (2)$$

where k is the number of enzymes per droplet, a_t is the mean amplification time, CV is the coefficient of variation on a_t and λ is the Poisson parameter computed from the fraction of positive droplets at $t = 150\ min$.

Statistics & Reproducibility

Experiments depicted in Figures 1 and 2 are all conducted as three technical replicates. Data are plotted as the mean values +/- the standard deviation. The amplification reactions were monitored for 1000 minutes (arbitrarily chosen). No data were excluded from the analyses. The specificity matrix (Figure 3) was assessed once. Digital enzyme counting (Figure 4) was performed from a minimum of three samples of different concentrations. For each data point, the error bar corresponds to the 95 % confidence interval.[66] The enzyme stock concentration (Figure 4E) was determined from a minimum of three measurements normalized by the dilution factor. Were excluded the measurements were the fraction of positive droplets exceeds 99 %, because of the high incertitude of the quantification. For time lapses, there is a tradeoff between the time frame interval (which related to the resolution of the distribution histograms) and the number of droplets that can be imaged (linked to the histogram precision). Given that it takes about 30 minutes for a droplet to go from a detectable amplifying signal to signal saturation, we set the time frame interval to 3 minutes (10 %). During such interval, about 10 frames of ~2000 droplets each (~20,000 droplets total) can be recorded (given our optical setup, field of view, illumination period, number of fluorescence channels…). Activity distributions from Figures 5-6 exclude droplets that do not correspond to the targeted diameter (due to droplet merging or instabilities during droplet generation) and droplets on the edges of the analyzed frames.

Data availability

The data that support the findings of this study are available within the paper and its Supplementary Information. All nucleic acid sequences and experimental conditions are available in the Supplementary Tables 1 and 3. Unprocessed data related to the Figure 1, 2 and 3 and 4 are provided in the source data file. Raw data (droplet coordinate and fluorescence for each time point) from the Figures 5 and 6 can be accessed at the following publicly accessible repository (doi: 10.5281/zenodo.10455918, 10.5281/zenodo.10455829 and 10.5281/zenodo.10455612).

Code availability

The Mathematica code used for droplet analysis is available via GihHub at the following link: https://github.com/GuGi75/Droplet-analysis

Methods-only references

63. Yamagata, A., Masui, R., Kakuta, Y., Kuramitsu, S. & Fukuyama, K. Overexpression, purification and characterization of RecJ protein from Thermus thermophilus HB8 and its core domain. Nucleic Acids Res 29, 4617–4624 (2001).
64. Menezes, R., Dramé-Maigné, A., Taly, V., Rondelez, Y. & Gines, G. Streamlined digital bioassays with a 3D printed sample changer. Analyst (2019) doi:10.1039/C9AN01744E.
65. Lobato-Dauzier, N. et al. Silicon chambers for enhanced incubation and imaging of microfluidic droplets. Lab on a Chip 23, 2854–2865 (2023).
66. Pekin, D. et al. Quantitative and sensitive detection of rare mutations using droplet-based microfluidics. Lab Chip 11, 2156–2166 (2011).